Prompt gamma rays detected with a BGO block Compton camera reveal range deviations of therapeutic proton beams

Hueso-González, F.; Pausch, G.; Petzoldt, J.; Römer, K. E.; Enghardt, W.;

Originally published:

January 2017

IEEE Transactions on Radiation and Plasma Medical Sciences 1(2017)1, 76-86

DOI: https://doi.org/10.1109/TNS.2016.2622162

Prompt gamma rays detected with a BGO block Compton camera reveal range deviations of therapeutic proton beams

F. Hueso-González, G. Pausch, J. Petzoldt, K. E. Römer, and W. Enghardt

***Abstract*—The dose deposition profile of protons is interesting for tumour treatment due to the increased ionization density at the end of their track. However, the inaccurate knowledge of the proton stopping point limits the precision of the therapy. Prompt gamma rays, a by-product of the irradiation, are candidates for an indirect measurement of the particle range. Compton cameras have been proposed for prompt gamma ray imaging, but struggle with high trigger rates and low coincident efficiency. The feasibility in a clinical environment has yet to be proved. At Universitäts Protonen Therapie Dresden, two bismuth germanate (BGO) block detectors arranged face-to-face are deployed for imaging tests with a homogeneous target irradiated by a proton pencil beam. Shifts of the target, increase of its thickness and beam energy variation experiments are conducted. Each measurement lasts about 15 minutes at a low proton beam current. The effect of one centimetre proton range deviations on the backprojected images is analysed. The number of valid Compton events as well as the trigger rate expected in a realistic treatment plan with pencil beam scanning are estimated. The results support the use of a high density material despite its moderate energy resolution, in order to maximize the coincident efficiency. Nevertheless, they discourage the applicability of a two-plane Compton camera in a clinical scenario with usual beam currents.**

***Index Terms*—proton therapy, range verification, prompt gamma ray imaging, Compton camera, BGO block detector.**

I. Introduction

ACCELERATED protons are outstanding particles for cancer treatment thanks to their finite range and the increase of the ionization density (the Bragg peak) close to the stopping point [1], [2], [3]. In theory, the dose can be concentrated on the tumour, while normal tissue is spared more efficiently than with traditional photon therapy. In practice, beam incidence directions stopping in front of an organ at risk cannot be exploited due to intrinsic proton range uncertainties. The Bragg peak position depends critically on tissue composition, which may change inadvertently between treatment fractions. This forces the application of broad safety margins [4] and field patching [5], and compromises to some extent the ultimate precision and aspirations of proton therapy.

Range verification in vivo and in real-time is imperative to detect severe range deviations with respect to the treatment plan and to improve the precision of the technique. Diverse experimental tools have been proposed during the last decades [5], but none is applied (widespread) in clinical routine yet. Significant efforts are focused on the imaging of prompt γ-rays: a secondary radiation with an emission distribution correlated to the proton dose deposition [6]. The energy spectrum of prompt γ-rays spans over a region of several MeV [7]. Gamma cameras used traditionally in nuclear medicine for lower energies cannot be used here, as the collimator and detector thickness would be insufficient. Systems based on passive (mechanical) collimation like the knife-edge shaped slit camera, specially designed for the current application, have proven the ability to detect millimetre range shifts at clinical currents [8] with heterogeneous phantoms [9] and even in patient treatments [10].

A Compton Camera (CC) [11] has been suggested for imaging prompt γ-rays in proton therapy [12], [13], [14], [15]. It is based on active (electronic) instead of passive collimation. A scatterer plane and an absorber detector, made both of materials with high energy and spatial resolution, as well as high scattering and photoabsorption efficiency, respectively, measure the energy deposit and γ-ray interaction position. Detector time resolution is also advisable for rejecting random coincidences. The scattering angle θ is related through the Compton equation [16] to the energies of the original (E_γ) and scattered ($E_\gamma{}'$) photons:

$$\begin{aligned} \cos\theta &= 1 - \mathrm{m_e c^2}\left(1/E_\gamma{}' - 1/E_\gamma\right) \\ E_\gamma &= L_\mathrm{s} + L_\mathrm{a} \\ E_\gamma{}' &= L_\mathrm{a} \end{aligned} \tag{1}$$

where $\mathrm{m_e c^2} = 511\,\mathrm{keV}$ is the electron rest energy, and L_s and L_a are the energies deposited in scatterer and absorber. Note that this formula holds if the incident γ-ray interacts just once in the first plane, and the scattered γ-ray is fully absorbed in the second plane. An iterative imaging algorithm reconstructs

F. Hueso-González and W. Enghardt are with Helmholtz-Zentrum Dresden-Rossendorf, Institute of Radiooncology, Bautzner Landstr. 400, 01328 Dresden, Germany.

K. E. Römer is with Helmholtz-Zentrum Dresden-Rossendorf, Institute of Radiation Physics, Bautzner Landstr. 400, 01328 Dresden, Germany.

J. Petzoldt, G. Pausch and W. Enghardt are with OncoRay - National Center for Radiation Research in Oncology, Faculty of Medicine and University Hospital Carl Gustav Carus, Technische Universität Dresden, Fetscherstr. 74, PF 41, 01307 Dresden, Germany.

W. Enghardt is also with Department of Radiation Oncology, Faculty of Medicine and University Hospital Carl Gustav Carus, Technische Universität Dresden, Fetscherstr. 74, 01307 Dresden, Germany, and with German Cancer Consortium (DKTK), and with German Cancer Research Center (DKFZ).

Current affiliation of F. Hueso-González is Target Systemelektronik GmbH, Heinz-Fangman-Straße 4, 42287 Wuppertal, Germany. J. Petzoldt is now with Advanced Technology Group, Ion Beam Applications SA, Chemin du Cyclotron 3, 1348 Louvain-la-Neuve, Belgium. Present affiliation of G. Pausch is Helmholtz-Zentrum Dresden-Rossendorf, Institute of Radiooncology, Bautzner Landstr. 400, 01328 Dresden, Germany.

Contact: Fernando.Hueso@OncoRay.de. This work was supported by the German Federal Ministry of Education and Research (BMBF-03Z1NN12) and the European Commission (FP7 Grant Agreement N. 264552).

the γ-ray origin if several events are accumulated [17].

The application of the two-plane CC for Prompt Gamma-ray Imaging (PGI) faces numerous field-specific problems [18]:

- The non-monoenergetic energy spectrum of prompt γ-rays does not allow for an easy correction of escape energy in the absorber.
- The high γ-ray energies (several MeV) of prominent characteristic lines lead to increased pair production and probability of escape energy [19].
- If the incident photon energy were fixed and known in advance, a good energy resolution in the scatterer would be sufficient. Alternatively, if full absorption were likely, an Energy Subtraction Compton Scatter Camera [20] with just good resolution in the absorber could be deployed. However, for PGI, the initial γ-ray energy is not fixed and full absorption is not guaranteed, so that a good energy resolution in the scatter detector and a moderate one in the absorber are indispensable for event reconstruction.
- The low coincident efficiency (valid Compton events per γ-ray) is in the order of 10^{-5} per emitted γ-ray.
- There is a large detector load (γ-ray flux) and single trigger rate with clinical proton beam currents, e.g. 600 kcps at 2 nA with the slit camera [8].
- The relatively small number of prompt γ-ray emissions per imaging voxel ($\sim 10^4\,/\,\mathrm{mm}^3$ on average in a 1 Gy treatment fraction), compared to the camera efficiency, limits the collected statistics and compromises the image resolution.
- There is an asymmetry between trigger rate in scatterer (thin) and absorber (thick) layer.
- A high radiation background is present due to scattered protons and neutrons, which produce γ-rays when captured in the patient or any surrounding materials.
- The elevated percentage of random coincidences degrades the quality of the reconstructed images.
- The required detector size and resolution, as well as number of electronic channels, increase critically the system price.

These complications, most of them yet unsolved, cast doubts on the applicability of this approach in a clinical scenario [21]. Spectral reconstruction or a three-layer camera [15], [22] have been proposed to compensate for missing energy and to avoid the trigger rate asymmetry, but its outcome and efficiency have to be proven, respectively. As a consequence, a camera prototype demonstrating range verification in a clinical scenario is still a challenge several institutes aim at [23], [24], [25], [26], [27], [28]. To the best of our knowledge, published experimental results of CCs with prompt γ-rays correspond to:

- 4.4 MeV γ-rays in a background-free and monoenergetic scenario [29].
- < 2 MeV γ-rays at a proton beam [13], [30], which have lower correlation to the range [7].
- > 2 MeV γ-rays at a research accelerator [31] and at a proton therapy facility [32], but with beam currents of around 10 pA at nozzle exit, far below the typical clinical value of 2 nA for treatment plans with the widespread Cyclone® 230 (C230) of IBA.

Is it then feasible at a clinical scenario? Or will the CC unfortunately be overwhelmed by a constant flow of background events in the different stages? – as raised by [21]. To answer this question, further experimental results on which to build upon are needed, that reject or confirm the worst expectations. Knowing all difficulties, it is of great importance to approach the problem step by step. First, the suitability in a clinical environment with realistic rates has to be assessed with the simplest methods and minimal efforts necessary. If the proof is successful, further complexity steps can be added to improve the camera efficiency (size) and its precision; the factors degrading the reconstructed images can be identified, and the reconstruction algorithm can be optimised. The other way round, it is difficult to find at which point of the chain it is failing or if it is not working from the very grounds.

II. Motivation

It is an established belief that an excellent energy resolution is required for the scatterer plane of the two-plane CC aiming at PGI. Crystals like CdZnTe [23], [28], Si [24], [26], [27] or $LaBr_3$:Ce [25] are deployed in current prototypes. Thin layers are preferred to position accurately the cone vertex and reduce photoabsorption and multiple scattering before reaching the absorber. In contrast, our idea is to use a 3 cm thick Bismuth Germanium Oxide - $Bi_4Ge_3O_{12}$ (BGO) block detector as scatterer. The use of BGO as scatterer was investigated already in [33] but had not been implemented experimentally to date.

At first sight, this choice may generate surprise due to the moderate energy resolution of this scintillator. However, the rationale is to obtain a higher incoherent scattering efficiency, which is proportional to the mass density [34, chapter 4] and increases with thickness. We maximise the efficiency instead of the energy (and spatial) resolution, and opt for the first factor of this trade-off, as opposed to the current trend. By choosing a denser (and cheaper) material such as BGO, one collects more events but with less precision. In addition, the trigger rate between stages is equalised.

Why is the efficiency a crucial factor? In the field of PGI, we measure a by-product of the proton irradiation, which is generated with a given rate and limited amount. On average, only one out of ten protons produces a prompt γ-ray [21]. To obtain a statistically significant image and detect local range shifts, enough γ-rays (Compton events) have to be collected. Taking into account the patient treatment constraints, a very precise but inefficient camera may not gather enough events per imaging voxel, and the image quality would be jeopardised.

III. Aim

This article presents the BGO block Compton camera (BbCc), a two-plane CC setup assembled at OncoRay, Universitäts Protonen Therapie Dresden (UPTD) and Helmholtz-Zentrum Dresden-Rossendorf (HZDR). It is based on two segmented BGO block detectors, for maximising the scattering efficiency and reducing the asymmetry between trigger rate in scatterer versus absorber. The goal is to obtain experimental

data with this simple camera at a proton beam, extending the few results already published in the literature. The specific questions to be answered are:

- Is the BbCc sensitive to 1 cm range shifts of a proton pencil beam in a homogeneous target for high energy prompt γ-rays, despite the moderate energy resolution of the scatterer stage and its large thickness?
- What coincident efficiency and single trigger rates of the BbCc are expected with clinical currents compared to other prototypes under development? Are the detectors and electronics able to sustain the γ-ray flux?
- How many detectors are required to detect 2 mm range shifts with statistical significance in a realistic treatment plan fraction with Pencil Beam Scanning (PBS)?

IV. Materials and Methods

The BbCc comprised two BGO block detectors from Siemens Positron Emission Tomography (PET) scanners. The scatterer was named as sBGO and had a size of 35.0 mm×37.5 mm×30.1 mm, the absorber was called[1] aBGO and its dimensions were 52.7 mm×52.7 mm×20.0 mm. Each crystal was segmented in an 8×8 matrix and coupled to four light-sharing Photomultiplier Tubes (PMTs) operated at +1350 V. In spite of its larger thickness, sBGO was chosen as scatterer due to its smaller crystal pitch and front face area. The blocks were arranged face-to-face and the distance between the respective crystal centres was ∼6.5 cm. The rationale for this orientation was to avoid any interfering material (PMT, electronic boards) between scatterer and absorber crystals (cf. fig. 1 (bottom), green area), so that the γ-rays scattered in the sBGO block did not undergo further interactions until reaching the aBGO detector. The choice of BGO instead of Cerium-doped lutetium oxyorthosilicate - Lu_2SiO_5:Ce (LSO) blocks is justified by the absence of intrinsic activity, lower price, as well as the comparable performance in the energy range of interest [35]. The signal processing was based on analog front-end VERSAmodule Eurocard (VME) electronics, which are described in [36].

The reason for the relatively high efficiency of this setup, concerning single events, is the dependence of the Compton attenuation coefficient σ on ρ/E_γ [34, chapter 4]. A very dense ($\rho_{\mathrm{BGO}} = 7.13\,\mathrm{g/cm^3}$) and thick (3 cm) scatterer was chosen to balance the high energy E_γ expected in the PGI field. CCs developed for low energies comprise scatterer planes with low density, which have a poor incoherent scattering efficiency in the high energy region. Due to the system price and the restricted space in the treatment room, the increase of just the detector area seems not an acceptable solution to improve the efficiency: alternative materials are needed. To give some numbers at 4.4 MeV γ-ray energy, the incoherent scattering efficiency $\epsilon_\sigma = 1 - \exp(-\sigma t)$, being t the scatterer thickness, yields 40 % for sBGO ($t = 3$ cm) compared to 20 % for each stage of the Polaris camera [32], made of $t = 1.5$ cm thick Cadmium zinc telluride - CdZnTe (CZT) detectors.

[1]The same detectors were named in previous publications as BGO4 and BGO1, respectively.

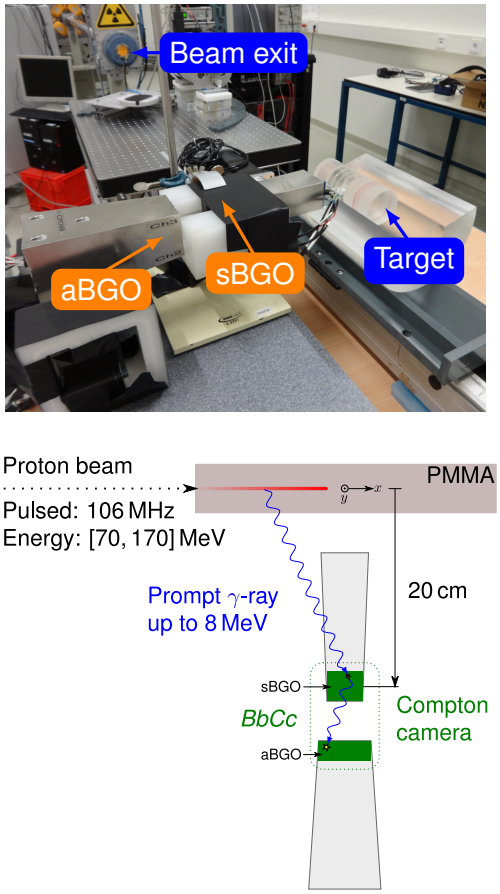

Figure 1: Photo and schematic top view of the BbCc setup at the experimental area of UPTD (C230 accelerator). The proton pencil beam, with an energy between 70 and 170 MeV, and a bunch repetition rate of 106 MHz, irradiates a Polymethyl Methacrylate - $[C_5O_2H_8]_n$ (PMMA) target. The BbCc setup (block detectors aBGO and sBGO) measures the prompt γ-rays (dynamic range up to 8 MeV). Real aspect ratio is preserved. The active detector area (crystals) is highlighted in green; the housing, PMT tubes and electronics are depicted in gray.

Before beam tests, the BbCc was characterised extensively in the laboratory, at HZDR and UPTD, with point-like photon sources: ^{22}Na (511 and 1275 keV), ^{60}Co (1173 and 1333 keV) and ^{242}Cm + ^{13}C (6130 keV)[2]. Specifically, the following experiments and measurements were performed:

- Energy resolution of each detector for the different photopeaks. The energy spectra of a ^{22}Na source and prompt γ-rays produced in a PMMA target by a 100 MeV proton beam are compared.
- Energy correlation spectra with the ^{22}Na source, once in front of the camera, once between the detectors.
- Spatial shifts of the point-like sources and analysis of the respective Back Projection (BP) images. Acquisition

[2]Curium emits α particles, that sometimes fuse with a carbon nucleus. The product is a neutron and ^{16}O* in an excited state, similar to that produced in proton reactions [37]. It deexcites via the emission of a 6.1 MeV prompt γ-ray.

of ^{22}Na line source measurements by periodic uniform motion of the point-like source.

Furthermore, the spatial and time resolution of each block detector (aBGO and sBGO) was measured as a function of photon energy at the Electron Linear accelerator for beams with high Brilliance and low Emittance (ELBE). The block detector calibration procedure, which includes pixel-wise energy and time calibration, and the energy resolution characterisation for different photopeaks between 511 keV and 4.4 MeV, as well as the spatial and time resolution measurements, are reported for aBGO in [35], [18]. Most results are also applicable for the sBGO detector and are thus not reported explicitly here.

Then, a measurement campaign at the horizontal pencil beam line (experimental area, no scanning) of UPTD was conducted. A homogeneous target was irradiated with low beam currents compared to therapy conditions, since the deployed acquisition system allowed only a relatively small throughput. The BbCc was placed perpendicularly to the beam axis at a distance of 20 cm, cf. fig. 1, and detected the produced prompt γ-rays. The homogeneous target was constructed out of cylindrical PMMA slices of 5 cm diameter and different thicknesses, and was mounted on a linear stage with remote control.

Three types of experiments were carried out for exploring the responsiveness of the camera to range deviations:

1) Shifts of a 2 cm thick PMMA target along the beam axis for 70 MeV protons.
2) Increase of the target thickness from 2 to 16 cm in 1 cm steps for 160 MeV protons.
3) Variation of the beam energy from 70 to 170 MeV in 10 MeV steps for a 40 cm thick target.

Each measurement point lasted around 15 min at a continuous beam current of $\sim$40 pA and an individual detector load of $\sim$50 kcps. The alignment of the detectors was performed with a self-levelling cross-line laser and the precision of the distance between detectors was not better than 4 mm.

The BbCc setup followed the *keep it simple* philosophy. It was a two-plane CC made of high efficiency but conventional and relatively cheap detectors. A custom routine based on the simple analytic BP method for two-plane events [17], [18], [38] was written on ROOT [39] for image reconstruction. The definition of the x and y axis, cf. fig. 1, is from the perspective of an observer standing behind the camera (looking at the source), so that the images are upright. The focus of the paper is set on experimental data (energy spectrum, trigger rates, simple BP images) rather than on the reconstruction itself. For simplicity, the sensitivity matrix was not taken into account, as it does not invalidate the manuscript conclusions. Also, the complexity of iterative algorithms is not confronted.

The measurements were done with low beam currents and long measurement times, in order to gather enough statistics to draw significant conclusions. It is expected that the images obtained with the BbCc at the UPTD proton beam reveal proton range shifts, at the price of bad resolution (precision). Then, one can assess (extrapolate) whether a sufficient amount of statistics would be collected in a realistic treatment plan, and the setup would sustain the expected γ-ray flux. These simple tests should be an indispensable precondition and guidance in the development of the CC.

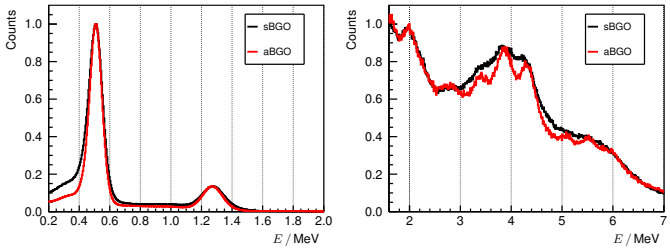

Figure 2: Detector response energy spectra of the scatterer (sBGO) and absorber (aBGO) of the BbCc at UPTD. Left: ^{22}Na point-like source. Profiles are normalised to the peak height at 511 keV. Right: prompt γ-rays emitted in a PMMA phantom when irradiated by a 100 MeV proton pencil beam. Profiles are normalised to the peak height at 2 MeV. Both: no explicit time filter is applied, see text.

V. Results

A. Energy resolution

In fig. 2, some representative detector energy spectra are shown for the scatterer (sBGO) and absorber (aBGO) of the BbCc. The energy resolution R_{E} at 511 keV is better for aBGO ($\sim$ 19 %) than for sBGO ($\sim$ 22 %). At the 1275 keV photopeak, one obtains 12 % and 13 %, respectively. This difference is more significant at 4.4 MeV, where the photopeak cannot be easily resolved from the Single and Double Escape Peaks (SDEP) for sBGO. The reason might be the smaller size of the sBGO pixels, which leads to larger electron escape probability, γ-ray absorption through multiple processes in two separate pixels (so that the spatial and pixel-wise energy calibration fail), and worse light collection from thin long crystals.

B. Energy correlation spectra

In fig. 3, one can see the correlation between the energy deposit at each block detector. In the left plot, the ^{22}Na source is located between both blocks (like a PET camera). In the right one, the source is not between blocks but in front of the scatterer (like a CC). In the case of PET, one can identify the uncorrelated 511 keV lines (one vertical, one horizontal), where just one detector absorbs a 511 keV photon, and the actual photopeak coincidences (hot spot) from the correlated back-to-back annihilation photons due to the emitted positrons. The scatter plot in the case of Compton imaging is different. Apart from the uncorrelated lines (vertical and horizontal), one can see diagonal strips. They correspond to real Compton events (scattered and absorbed photons) in the camera, stemming from the 511 and 1275 keV γ-rays. Mathematically, these straight lines are expressed by the implicit equation $E_{\mathrm{aBGO}} + E_{\mathrm{sBGO}} = E_{\gamma}$. These may also appear in fig. 3 (left) due to backscattering, but are suppressed compared to single events and PET coincidences.

It is worth noting that no time filter is applied explicitly in the presented results, meaning that no cut is set on the coincidence time spectrum. The rationale is to recover events

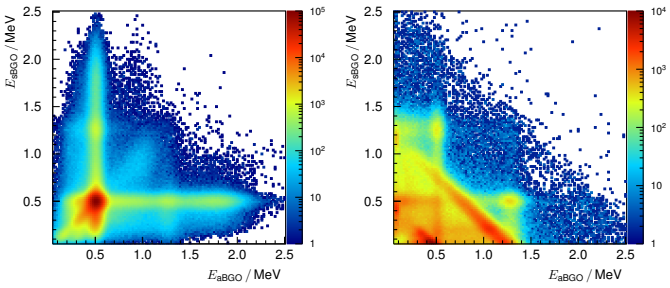

Figure 3: Energy scatter plots of the BbCc camera for a ^{22}Na point-like source. No explicit time filter is applied, see text. Left: the source is located between both block detectors (PET camera). Right: the source is in front of both blocks (Compton imaging). Both: color scale is arbitrary.

where one of both detector signals is under the discriminator threshold, so that its time stamp is missing, but a valid (small) energy is measured. The trigger is produced by the other block detector, and the same integration gate is used for both. The condition of positive energy implies an indirect time filter, as broad as the integration window. Thus, more events are recovered at the price of a higher number of random coincidences. This strategy has more or less impact on the image quality depending on the detector rate.

C. BP images of radioactive sources

Fig. 4 (top left) depicts the BP images of a ^{22}Na photon source placed in front of the BbCc. The Full Width at Half Maximum (FWHM) is $\sim$5 cm in each spatial dimension. Fig. 4 (top right) corresponds to a 10 cm ^{22}Na line source (along x), whereas the bottom row is obtained with 30 cm line sources at different heights (y axis).

In the reconstructed image profiles of fig. 5, the effect of spatial shifts along the x axis is observed. The left plot corresponds to a ^{60}Co source. The right one, to a ^{242}Cm + ^{13}C source.

D. Proton beam

At UPTD, a 70 MeV proton pencil beam irradiates a thick homogeneous target, and the resulting prompt γ-ray distribution is measured with the BbCc setup. The energy correlation spectrum is shown in fig. 6 (left), whereas the energy sum is depicted in fig. 6 (right), showing a broad peak at the 4.4 MeV energy region. Resolving the photopeak from the SDEP is not expected due to the insufficient energy resolution of the individual detectors, cf. fig. 2 (right).

In fig. 7, the image of a prompt γ-ray distribution produced by a 70 MeV (left) and 160 MeV (right) proton pencil beam irradiating a homogeneous PMMA phantom is shown. Note that an energy filter between 1.0 and 6.0 MeV is applied, to enclose the region seen in fig. 6 (right). The resulting number of valid coincidences after application of different filters is detailed for fig. 7 (right) in table I.

Fig. 8 shows the effect on BP profiles of spatial shifts of a ^{22}Na source (left), and of prompt γ-rays (right) produced by a 70 MeV proton pencil beam irradiating a thin PMMA target.

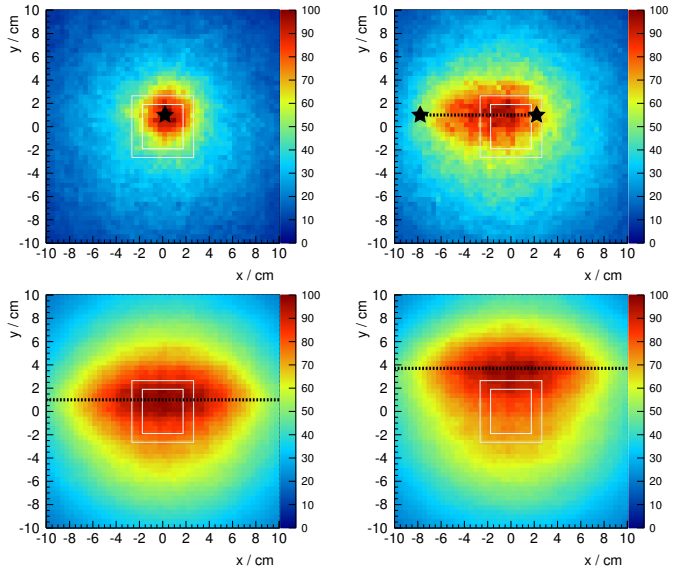

Figure 4: BP images of the BbCc at UPTD with a 1275 keV source. Its distance to the scatterer centre is (18.0 $\pm$ 0.9) cm. The distance between scatterer and absorber centres is (6.5 $\pm$ 0.4) cm. The white rectangles represent the front faces of sBGO and aBGO in the centre of the field of view. Top left: the black star is the expected position of the point-like source. About 9000 coincidences are used for the BP. Top right: a 10 cm line source is produced by periodic motion of the source across the dashed line (between the two black stars). Close to 13000 events are accumulated. Bottom row: 30 cm line source (see dashed line, black stars are out of the histogram range) at different heights (y axis) with respect to the camera; each image accumulates $\sim$ 350000 Compton cone projections. All: color scale is arbitrary.

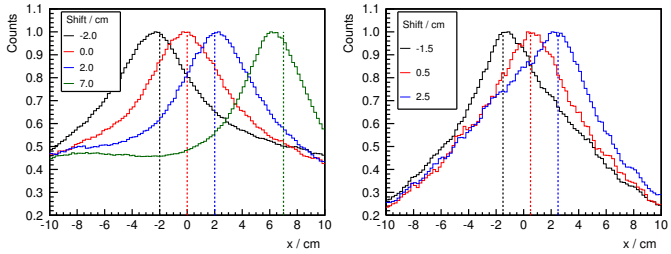

Figure 5: BP profiles of the BbCc for the spatial shift experiment at HZDR (across the x axis). Left: ^{60}Co point-like source (energy filter around the two photopeaks). Each BP is performed with $\sim$ 100000 events. Right: 6.1 MeV γ-rays (energy filter includes the SDEP) produced by a ^{242}Cm + ^{13}C source. About 20000 coincidences are accumulated for each position. Both: profiles are normalised to their respective maximum. The dashed lines represent the performed source shift. The distance between source and centre of the scatterer is (19.6 $\pm$ 0.9) cm; between scatterer and absorber centres, it is (6.8 $\pm$ 0.4) cm.

Table I: Valid Compton events for a particular experiment at a 160 MeV proton pencil beam with the BbCc setup and a homogeneous 40 cm thick PMMA phantom.

Applied filters	Valid events	k_ϵ
$E_{i\mathrm{BGO}} \in [0.05, 6]$ MeV; $E_{\mathrm{sum}} \in [1, 6]$ MeV	280×10^3	4.1 %
$E_{i\mathrm{BGO}} \in [0.05, 5]$ MeV; $E_{\mathrm{sum}} \in [3, 5]$ MeV	130×10^3	1.9 %
$\lvert t_{\mathrm{aBGO}} - t_{\mathrm{sBGO}}\rvert < 20$ ns; $E_{i\mathrm{BGO}} \in [0.05, 6]$ MeV; $E_{\mathrm{sum}} \in [1, 6]$ MeV	85×10^3	1.3 %
$\lvert t_{\mathrm{aBGO}} - t_{\mathrm{sBGO}}\rvert < 20$ ns; $E_{i\mathrm{BGO}} \in [0.05, 5]$ MeV; $E_{\mathrm{sum}} \in [3, 5]$ MeV	28×10^3	0.4 %

Note: the experiment corresponds to the BP image of fig. 7 (right). Depending on the applied coincidence filters, a different number of events usable by the image reconstruction algorithm is obtained. $E_{i\mathrm{BGO}}$ refers to the energy deposit at each block detector ($i = \mathrm{s}, \mathrm{a}$). $E_{\mathrm{sum}} \equiv E_{\mathrm{sBGO}} + E_{\mathrm{aBGO}}$. k_ϵ is the ratio between valid events and the number of hits acquired by the sBGO detector (6.8×10^6).

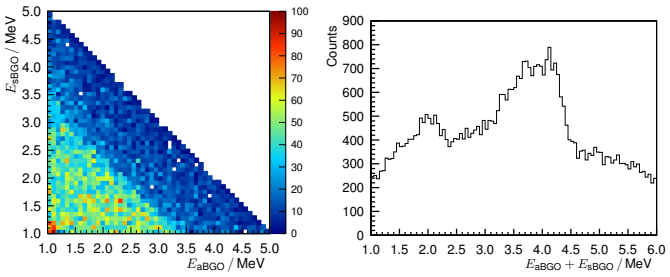

Figure 6: The BbCc measures at UPTD prompt γ-rays produced within a homogeneous PMMA phantom by a 70 MeV proton pencil beam. Here, coincident events are selected based on a broad time window of 40 ns and a filter on the sum of energies of both detectors between 1.0 and 6.0 MeV, see third filter of table I. Left: energy correlation spectrum. Color scale is arbitrary. Right: energy sum spectrum.

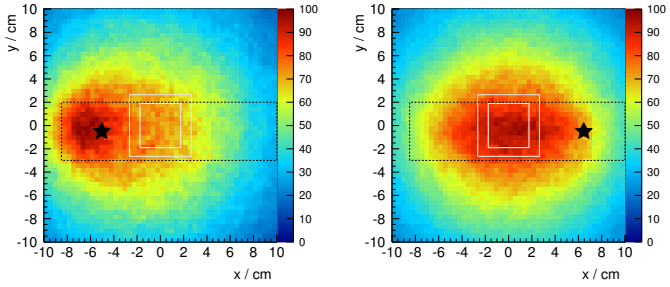

Figure 7: BP images of the BbCc at UPTD corresponding to prompt γ-rays produced by protons irradiating a homogeneous PMMA phantom. Beam incidence is from the left. The distance between beam axis and scatterer centre is (20.0±0.9) cm; between crystal centres, it is (6.5 ± 0.4) cm. The white rectangles represent the front faces of sBGO and aBGO in the centre of the field of view. The dashed black rectangle represents the target size ($\varnothing$ 5 cm×40 cm) and the black star, the expected proton range in PMMA. It yields 3.5 cm for 70 MeV (left) and 15.1 cm for 160 MeV (right) protons. The third filter of table I is applied. Color scale is arbitrary. The left image contains $\sim$40000 coincidences; the right one $\sim$85000.

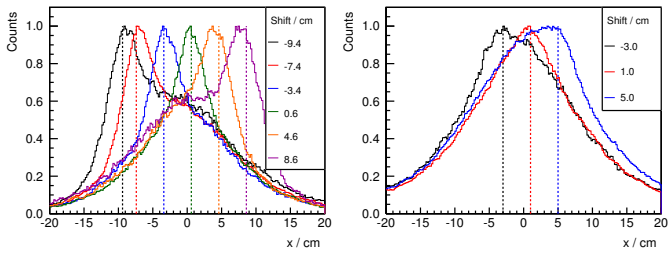

Figure 8: BP profiles of the BbCc for the spatial shift experiment at UPTD. Left: ^{22}Na point-like source (energy filter around the 1275 keV photopeak). The distance between motion axis and scatterer centre is (18.0 ± 0.9) cm. Right: prompt γ-rays (third filter of table I is applied) produced by 70 MeV protons crossing a thin PMMA phantom ($\varnothing$ 5 cm×2 cm). Beam incidence is from the left. Profiles are normalised to their respective maximum. The dashed lines represent the performed shift of the source (left) or of the target (right). The distance between motion axis and scatterer centre is (20.0 ± 0.9) cm. Both: the distance between crystal centres is (6.5 ± 0.4) cm. Each BP profile contains $\sim$10000 Compton cones.

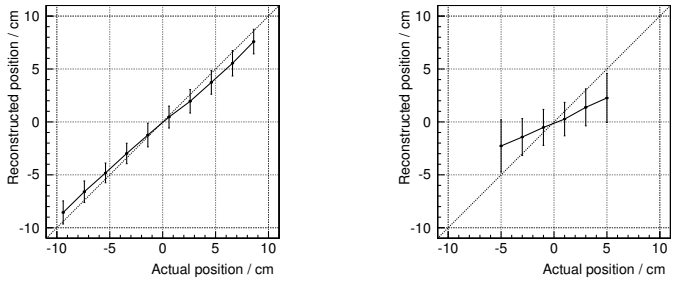

Figure 9: Left: centroid of the reconstructed profiles (among others) of fig. 8 (left) versus the actual position of the ^{22}Na point-like source (1275 keV photopeak). Right: analogous plot for prompt γ-rays produced inside the thin PMMA phantom, cf. fig. 8 (right). Both: the fit function for obtaining the centroid parameter and its error is a Pseudo-Voigt profile. The diagonal grid line depicts the ideal point distribution.

The source/target spatial shift is correlated with a change of the mean value of the distribution. The analysis of the centroid of the distribution over the actually performed shift is depicted in fig. 9. For the left graph, there is a good agreement between the measured points and the ideal position; for the right case, one can see a trend but no quantitative match.

The profile asymmetry observed for point-like sources located off the central axis ($x \neq 0$), cf. figs. 5 and 8 (left), may be due to the absence of a sensitivity correction in the image reconstruction algorithm (simple BP).

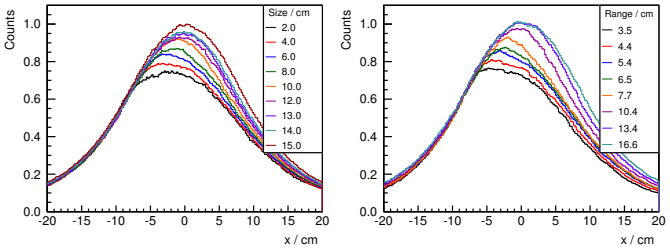

Figure 10: BP profiles of the BbCc for prompt γ-rays at UPTD. The beam axis is (20.0 ± 0.9) cm away from the scatterer centre, the distance between scatterer and absorber centres is (6.5 ± 0.4) cm. Beam incidence is from the left. The front face of the PMMA target is fixed in all cases at $x \simeq -9$ cm, cf. black dashed rectangle in fig. 7. Normalisation is done empirically to match all distributions at this spatial point. The third filter of table I is applied. Left: increasing the PMMA target thickness for 160 MeV protons (15.1 cm range). Proton range exceeds the thickness of the target for all measurements. Right: varying the proton beam energy (range) in 10 MeV steps from 70 to 170 MeV for a thick PMMA phantom ($\varnothing$ 5 cm$\times$40 cm). Both: each BP profile contains $\sim$50000 coincidences. Some thicknesses (left) and ranges (right) are excluded for the sake of clarity.

BP profiles of prompt γ-rays produced in targets of various thicknesses by a 160 MeV proton beam are compared in fig. 10 (left). Fig. 10 (right) shows the complementary experiment with a fixed thickness PMMA target, but increasing the initial proton energy from 70 MeV up to 170 MeV. In both cases, a shift to the right in the mean value of the distribution can be identified correlated with the spatial range of γ-ray emission.

VI. Discussion

A. General remarks

Target shifts, thickness increase or beam energy variation, corresponding to range differences down to 1 cm, correlate to visible changes of the BP images. These results highlight the ability of the BbCc setup, comprising just eight electronic channels, to obtain images of high energy prompt γ-rays, despite the moderate energy resolution of BGO.

Together with [32], this paper yields one of the first experimental results of CCs at 4.4 MeV at a proton pencil beam of a clinical facility. In both cases, the beam currents are far below the clinical values. The main difference is that [32] used CdZnTe semiconductor detectors with better energy resolution, but less density than BGO, and a scatterer with 1.5 cm thickness instead of the 3.0 cm of sBGO.

As a side note, BGO is used as scatterer instead of LSO, despite the better energy resolution of the latter and similar scattering efficiency, in order to avoid the problem of trojan coincidences discussed in [35]. This choice is endorsed by the comparable performance of BGO and LSO in the PGI energy range (high γ-ray energies). The intrinsic background of LSO is a too high price to pay for a small increase in energy resolution, that is wasted anyway in the case of events with incomplete energy deposition or unstable gain.

B. Rate, efficiency, statistics and clinical parameters

Let us now address the questions concerning detector rate, efficiency and collected statistics of PGI CCs in the clinics. First, we describe several factors of relevance:

- Beam current: the instantaneous proton current at nozzle exit during spot delivery in a PBS treatment plan. It is about 2 nA for the C230 cyclotron, not to mistake with the current at extraction radius nor with the average current including the dead time due to layer changing and magnet tuning [40].
- Spot duration T_{spot}: the temporal length of a single spot of a treatment plan in PBS. It can be up to several milliseconds, the strongest spot containing $\sim 10^8$ protons [41, fig. 19]. The number of protons per spot is (generally) proportional to the spot duration, as the beam current is kept constant at 2 nA, except for spots with very low dose.
- Detector load $\dot{N}_{\text{load}}$: the particles interacting in the detector per unit time (producing a measurable scintillation pulse). The upper limit is given by the tolerable pile-up for the particular crystal (and PMT space charge effects).
- Trigger rate $\dot{N}_{\text{trig}}$: those detector pulses above a specified signal (energy) threshold set in the hardware.
- Event throughput $\dot{N}_{\text{through}}$: those trigger events processed by the data acquisition. The limit depends on the electronics and acquisition dead time. In any case, $\dot{N}_{\text{load}} \geq \dot{N}_{\text{trig}} \geq \dot{N}_{\text{through}}$. For high trigger rates, $\dot{N}_{\text{through}} \ll \dot{N}_{\text{trig}}$.
- Load asymmetry: difference between the detector load in the scatterer and absorber of the CC.
- Coincident efficiency k_ϵ: not all γ-rays interacting in the scatterer will reach and interact with the absorber, just a small percentage k_ϵ will result in a trigger coincidence.
- Background rate: scattered protons, activated nuclei or neutrons lead to an additional detector load and real coincidences, but from γ-rays of no interest. Correlation with the beam Radio Frequency (RF) can be used for background suppression [42], but is not applied here.
- Random coincidences: the higher the detector load and the worse the detector time resolution, the larger the probability of considering two independent interactions in scatterer and absorber as a coincidence.

In summary, detectors deployed in the PGI field, and especially CCs, face a complex and multi-factorial problem. The beam current and spot duration are fixed parameters in the clinics, so that the produced number and rate of γ-rays is limited. It is important to measure as many of them as possible, but without surpassing the maximum detector load $\dot{N}_{\text{load}}$. To gather enough statistics per spot, the event throughput has to be as high as possible ($\dot{N}_{\text{through}} \to \dot{N}_{\text{trig}}$), i.e. the dead time has to be minimized. Furthermore, it is advisable to have a comparable trigger rate in each stage, so that the coincident efficiency of the camera is maximum but the load in the absorber is not compromised.

C. Efficiency of the BbCc setup

Considering now the unoptimised BbCc setup in the current experiment, cf. fig. 1, the ratio k_ϵ between valid Compton events and the single trigger rate at the scatterer is analysed.

A particular measurement is chosen, namely an irradiation of a (40.0 ± 0.1) cm thick PMMA phantom $\varnothing\,(5.0 \pm 0.1)$ cm with (160 ± 3) MeV protons [43], i.e. (15.1 ± 0.2) cm range. The individual detector trigger rate is (90 ± 5) kcps for sBGO and (70 ± 5) kcps for aBGO, arranged as depicted in fig. 1. The measurement lasts (7.0 ± 0.1) min and the dynamic dead time of the VME data acquisition is $(85 \pm 5)\,\%$. The number of hits acquired and processed is $(6.8 \pm 0.1) \times 10^6$ for sBGO and $(3.4 \pm 0.1) \times 10^6$ for aBGO. The number of valid Compton events depends on the condition set for the coincidence, cf. table I for different filters, and the values for k_ϵ range between 0.4 % and 4.1 %.

What is the situation in a clinical irradiation scenario (PBS treatment plan at the C230 accelerator)? The beam current is around ~ 2 nA, i.e. 1.2×10^{10} protons per second (measured at nozzle exit). The strongest spot may last up to 8 ms. If the sBGO detector is placed at 25 cm distance from the beam axis, the covered solid angle $\Omega/4\pi|_\mathrm{s}$ is 1.7×10^{-3}. Assuming a prompt γ-ray yield of $0.16\,\gamma/\mathrm{p}$ (γ-rays per proton) as in [44], 45 % average attenuation in the phantom above 1 MeV, and 56 % total detection efficiency at 4.44 MeV [45], the number of registered γ-rays per proton $\epsilon_{\mathrm{p}\gamma} \simeq 8.4 \times 10^{-5}$. The estimated detector trigger rate is about 1 Mcps (above 1 MeV, but far more if lower energies are included). Taking from table I an average factor $k_\epsilon \sim 2\,\%$, and dismissing the fact that BGO cannot sustain such detector load, this would lead to 20 kcps coincident rate (including also multiple scattering). Hence, for the longest spot, around 160 coincidences would be collected. This implies that a dosimetry based on each pencil beam spot is not feasible even with this efficient camera setup; one should increase the number of detectors considerably to obtain statistically significant conclusions.

D. Coincident efficiency of a two-plane CC

Let us derive a theoretical estimate of the expected coincident efficiency of a two-layer CC. Keeping in mind that it is all about the order of magnitude, we can draw some simple models based on rough approximations. These calculations are a good practice and can serve as a preliminary step, cross-check or even guidance of a future Monte Carlo (MC) simulation, which is more powerful but less handy. We assume a point-like source of 4.44 MeV prompt γ-rays at a distance d of the scatterer layer, with a circular front face of radius r and thickness t. The covered solid angle is $\Omega/4\pi|_\mathrm{s} = 0.5(1 - (1 + (r/d)^2)^{-0.5})$. For simplicity, the γ-ray incidence is perpendicular to the front face, and the crystal edges are neglected. The probability of undergoing at least one interaction is $\epsilon_\mu(t) = 1 - \exp(-\mu t)$, where μ is the linear attenuation coefficient. The incoherent scattering efficiency is $\epsilon_\sigma(t) = 1 - \exp(-\sigma t)$. What is the exclusive probability of undergoing one incoherent scattering but no other interaction? Dismissing the change of direction and of energy, the single scattering efficiency is $\epsilon_{1\sigma}(t) = \sigma t \exp(-\mu t)$. This function is zero at $t = 0$ and $t \to \infty$, and reaches a maximum at $t_\mathrm{max} = 1/\mu$. Increasing the scatterer thickness above t_max does not increment further the single scattering efficiency, as multiple scattering, photoabsorption and pair production reduce the number of valid events. In table II, the incoherent scattering efficiency is analysed for several CCs. The BbCc has the largest value of $\epsilon_{1\sigma}(t)$ compared to the available Polaris and Macaco cameras, made of CZT and $LaBr_3$ respectively. A virtual CC made of high density and fast scintillators like Cerium-doped gadolinium oxyorthosilicate - Gd_2SiO_5:Ce (GSO) or CeF_3 is also reported for comparison. For the BbCc, the thickness t is closest to t_max, so that $\epsilon_{1\sigma}$ is close to its maximum at a realistic (compact) size. Other effects like resolution loss due to depth of interaction, background radiation, non-monoenergetic energy spectrum or discriminator threshold are not explored here in dependence of t. For example, a thick scatterer without information about the depth of interaction degrades considerably the image resolution as the apex of the cone is not placed in space as accurately as with a thin scatterer.

To derive roughly the number of valid coincidences per proton $\epsilon_{\mathrm{p,c}}$, we have to incorporate the absorber layer. The solid angle covered by the absorber $\Omega/4\pi|_\mathrm{a,s}$ can be obtained relative to the scatterer taking into account their distance $d_\mathrm{a,s}$. As the emission of scattered γ-rays is not isotropic but forward-peaked [18, subsection 2.1.1], we apply an arbitrary 1.5 correction factor on the solid angle. The detection efficiency ϵ_μ in the absorber is calculated with the total attenuation coefficient. Finally, $\epsilon_{\mathrm{p,c}} \approx 0.16, \gamma/\mathrm{p} \times 0.55 \times \Omega/4\pi|_\mathrm{s} \times \epsilon_{1\sigma}(t) \times \Omega/4\pi|_\mathrm{a,s} \times 1.5 \times \epsilon_\mu \approx 0.16\,\gamma/\mathrm{p} \times 0.55 \times \Omega/4\pi|_\mathrm{s} \times \epsilon_{1\sigma}(t) \times k_\epsilon$.

E. Requirements for a clinical CC

Having scatterer layers and absorbers of reasonable size and separation, as deployed in current prototypes, $\epsilon_{\mathrm{p,c}}$ yields $\sim 10^{-6}$, cf. table III. We take now as example a 1 Gy treatment field of a brain tumour, with an irradiation volume of 8 cm×8 cm×15 cm and 9.3×10^{10} delivered protons, i.e. about 10^5 protons per mm^3 and Gy. One could then divide the irradiated region in 1.2×10^5 imaging voxels of 2 mm×2 mm×2 mm dimension. To detect 2 mm local range shifts with significance based on distribution shifts, one may require to accumulate at least 20 Compton cones per imaging voxel (assuming for simplicity a homogeneous event distribution within the grid), so that the statistical (Poisson) noise is below 25 %. To reach this goal with the BbCc, one would need to operate about 30 absorber-scatterer pairs (cameras). $\epsilon_{\mathrm{p,c}}$ is maximum compared to other prototypes, but the detector load is not sustainable due to the long decay time of BGO. Other dense scintillators like GSO or CeF_3 would be good alternatives, as their shorter decay times reduce the pile-up probability, and the overall efficiency can be increased, cf. table III.

F. Limitations and closing remarks

It is worth remembering the weaknesses or limitations of both the experimental setup and the presented results:

- The geometry and detector size are not optimised for a CC, it just deploys conventional block detectors available in our laboratory put face-to-face at a reasonable distance. A more thorough analysis of the efficiency of a CC and optimum layer thicknesses and compositions is given in [33].

Table II: Incoherent scattering efficiency of the first scatterer layer of different CCs for PGI.

Scatterer	$h \times w \times t$ / cm^3	$\Omega/4\pi\vert_s$	ρ / g/cm^3	σ / cm^{-1}	μ / cm^{-1}	ϵ_σ	ϵ_μ	$\epsilon_{1\sigma}(t)$	$1/\mu$ / cm	$\epsilon_{1\sigma}(1/\mu)$	$\dot{N}_{\text{trig}}$ / Mcps	$(10\tau)^{-1}$ / Mcps
BGO	3.5×3.8×3.0	0.17 %	7.13	0.16	0.28	39 %	56 %	21 %	3.6	22 %	1.04	0.33
CZT	4.0×4.0×1.5	0.20 %	5.78	0.13	0.20	18 %	26 %	15 %	5.0	24 %	0.14	0.33
$LaBr_3$	2.7×2.7×0.5	0.09 %	5.30	0.12	0.18	6 %	9 %	6 %	5.5	25 %	0.09	2.86
GSO	5.2×5.2×3.0	0.34 %	6.71	0.16	0.24	37 %	52 %	23 %	4.1	24 %	1.93	2.00
CeF_3	5.2×5.2×3.0	0.34 %	6.16	0.14	0.21	35 %	47 %	23 %	4.7	25 %	1.76	3.33

Note: BGO stands for BbCc, CZT for Polaris [32], $LaBr_3$ for MACACO [46] and GSO or CeF_3 for a virtual crystal, for comparison. The scatterer layer is assumed to be at $d = 25$ cm distance from the central axis of a homogeneous PMMA target, which is irradiated by a 160 MeV proton pencil beam. h, w and t are the height, width and thickness of the crystal. The covered solid angle $\Omega/4\pi|_s$ is approximated for a point source and a circular detector front face with radius $r = \sqrt{hw/\pi}$. ρ refers to the mass density, σ to the incoherent scattering coefficient and μ to the total linear attenuation coefficient. They are taken from [45] for a fixed prompt γ-ray energy of 4.44 MeV. $\epsilon_\sigma = 1 - \exp(-\sigma t)$, $\epsilon_\mu = 1 - \exp(-\mu t)$ refer to the incoherent scattering and total interaction efficiency, respectively. $\epsilon_{1\sigma}(t) = \sigma t \exp(-\mu t)$ is the probability of having just a single incoherent scattering interaction for the given crystal, see text. Its maximum value $\epsilon_{1\sigma}(1/\mu)$ is obtained for a virtual crystal with thickness $t_{\max} = 1/\mu$. $\dot{N}_{\text{trig}}$ is the expected trigger rate above 1 MeV with a 2 nA proton beam (measured at nozzle exit), a prompt γ-ray yield of $0.16\,\gamma$/p as in [44] and 45% attenuation in the target. In the case of CZT, $\dot{N}_{\text{trig}}$ is divided by four, as the layer consists of four separate detectors. $(10\tau)^{-1}$ is an estimate of the maximum detector load supported per crystal. Errors are not specified for the sake of clarity.

Table III: Detection efficiency of the absorber layer and coincidence rate of different CCs for PGI.

Absorber	$h \times w \times t$ / cm^3	$d_{a,s}$ / cm	$\Omega/4\pi\vert_a$	$\Omega/4\pi\vert_{a,s}$	ϵ_μ	$\dot{N}_{\text{trig}}$ / Mcps	k_ϵ	$\epsilon_{p,c}\times10^6$	Coincidences	Cameras
BGO	5.2×5.2×2.0	6.5	0.22 %	4.4 %	42 %	1.01	2.8 %	0.89	0.69	30
CZT	4.0×4.0×1.5	12.8	0.09 %	0.8 %	26 %	0.06	0.3 %	0.08	0.06	330
$LaBr_3$	3.2×3.6×1.0	4.0	0.11 %	4.9 %	17 %	0.20	1.2 %	0.06	0.04	470
GSO	5.2×5.2×3.0	5.0	0.24 %	6.9 %	52 %	1.34	5.3 %	3.62	2.81	10
CeF_3	5.2×5.2×3.0	5.0	0.24 %	6.9 %	49 %	1.27	5.0 %	3.43	2.65	10

Note: BGO stands for BbCc, CZT for Polaris [32], $LaBr_3$ for MACACO [46] and GSO or CeF_3 for a virtual crystal, for comparison. The scatterer layer is described in table II. The absorber stage is assumed to be at a distance $d_{a,s}$ from the scatterer, as reported by the respective experiments. h, w and t are the height, width and thickness of the crystal. The covered solid angle $\Omega/4\pi$ is calculated with respect to the distance to the beam axis ($d + d_{a,s}$) and $\Omega/4\pi|_{a,s}$ with respect to the scatterer, using the point source approximation and a circular detector front face with radius $r = \sqrt{hw/\pi}$. $\epsilon_\mu = 1 - \exp(-\mu t)$ is the total interaction efficiency, calculated for 4.44 MeV γ-ray energy. $\dot{N}_{\text{trig}}$ is the expected trigger rate above 1 MeV with a 2 nA proton beam (measured at nozzle exit), a prompt γ-ray yield of $0.16\,\gamma$/p as in [44] and 45% attenuation in the target. In the case of CZT, $\dot{N}_{\text{trig}}$ is divided by four, as the layer consists of four separate detectors. k_ϵ is the probability of having an interaction in the absorber for each scattered γ-ray. It is estimated as the product of $\Omega/4\pi|_{a,s}$, ϵ_μ and an arbitrary 1.5 correction factor in order to account for the forward-peaked distribution of Compton scattered γ-rays. The value obtained for the BbCc is in the same order of magnitude as those reported in table I. $\epsilon_{p,c}$ is an estimate of the number of valid coincidences per proton, see text. *Coincidences* refers to the number of Compton events collected (on average) by the camera in each 2 mm×2 mm×2 mm imaging voxel, for a 1 Gy treatment fraction with 9.3×10^{10} protons, an irradiated volume of 8 cm×8 cm×15 cm, and the given $\epsilon_{p,c}$. *Cameras* stands for the number of cameras (scatterer and absorber pairs) that would be needed in order to collect 20 coincidences per imaging voxel and a single 1 Gy treatment field. Errors are not specified for the sake of clarity.

- The proton beam current is far below the usual values, no PBS is applied and just homogeneous targets are explored.
- The normalisation of the profiles is done arbitrarily (matching by hand the leading edges), as no charge monitor is available during the experiments.
- No iterative reconstruction algorithm, including the detector response matrix, has been used.
- Changes of the BP images are not assessed quantitatively.
- Estimates of current, detector load and efficiency are rough order of magnitudes. Also, the maximum detector load assumed does not include phenomena like PMT space charge effects and gain drift [47].

Nonetheless, the specific conclusions drawn from the results are still valid. Hence, we do not plan to optimize the BbCc setup in the future or develop complex reconstruction algorithms, as this is not the focus and does not change the final statements. This provisional setup serves to demonstrate with the simplest means (conventional detectors and electronics) within our grasp and minimum effort that PGI Compton imaging is possible also with lower energy resolution but higher efficiency materials. Note also that we do not claim that BGO should be used necessarily as scintillation material in a CC (because of its long decay time). Rather, we challenge the beliefs by showing that higher efficiency and thickness instead of higher energy and spatial resolution is a way worth investigating.

Of course, there is a balance between the larger statistics due to higher density materials and the poorer angular uncertainty due to worse detector resolution [48]. The question whether a given range precision can be achieved with more events with less precision or few with higher is not answered quantitatively here. We just conclude that even with a high efficiency scatterer, the collected statistics in a clinical scenario seem more than one order of magnitude below what would be

advisable, or that the number of detectors should be increased by 30, or that unthought geometries and novel materials have to be deployed instead. In this context, other PGI systems like a slit camera or the prompt γ-ray timing method [44] might be more appropriate for proton range verification [18, section 4], due to their higher efficiency (no need for coincidences), lower cost and comparable precision.

VII. Conclusions

A slight scepticism has settled down in the scientific community concerning CCs for PGI. Due to technical complexity, electronics expense, load asymmetry between stages, low coincident efficiency, uncommon energy range (several MeV), high detector load, radiation background and the elevated percentage of random coincidences, only few experimental results hint at their applicability in a clinical environment. To close this gap, a high efficiency CC setup, made of standard PET block detectors, is used to measure 4.4 MeV prompt γ-rays produced in a PMMA phantom when irradiated by a proton pencil beam. Low currents are chosen to adapt the count rate to the low throughput of the acquisition system, and long measurement times are selected for gathering enough statistics to draw significant conclusions.

The analysis of the BP images gives evidence that 1 cm range variations in homogeneous phantoms can be detected when delivering a spot with $\sim 10^{11}$ protons at about 40 pA and measuring the resulting 4.4 MeV prompt γ-rays, as shown also by [32], but using here a 3 cm thick BGO as scatterer. This indicates that Compton imaging generally works with prompt γ-rays in a proton therapy accelerator, but under controlled conditions (current and phantom), and that higher efficiency and thicker materials could be favoured at the price of lower energy and spatial resolution.

Although there is no *theoretical* obstacle preventing CCs to be applied academically for prompt γ-rays, there are *practical* limitations questioning its feasibility as in vivo real-time range verification in the clinics. The high detector load and scarce statistics collected per pencil beam or per imaging voxel (based on estimates with clinical currents) make this approach for millimetre real-time range verification almost hopeless with a realistic treatment plan and current detectors and electronics technology. These intrinsic hurdles seem to be nowadays insurmountable if the usual beam current is not reduced. Moreover, one has to ponder if the electronics and operation complexity is worth the effort compared to other simpler PGI methods. In fact, due to the higher efficiency and lower expense, the prompt γ-ray timing or the slit camera may be the way to go for clinical translation in the future.

Acknowledgement

We thank M. Berthel, A. Dreyer, F. Fiedler, C. Golnik, K. Heidel, S. Helmbrecht, M. Iltzsche, T. Kormoll, S. Löck, L. Nenoff, M. Priegnitz, S. Schöne, M. Sobiella, A. Wagner and D. Weinberger for the excellent support and the crew of the ELBE and UPTD accelerator for stable operations.

References

[1] R. R. Wilson, "Radiological use of fast protons," *Radiology*, vol. 47, no. 5, p. 487, 1946. Available: http://dx.doi.org/10.1148/47.5.487

[2] W. D. Newhauser and R. Zhang, "The physics of proton therapy," *Phys. Med. Biol.*, vol. 60, no. 8, p. R155, 2015. Available: http://dx.doi.org/10.1088/0031-9155/60/8/R155

[3] M. Durante and H. Paganetti, "Nuclear physics in particle therapy: a review," *Reports on Progress in Physics*, vol. 79, no. 9, p. 096702, 2016. Available: http://dx.doi.org/10.1088/0034-4885/79/9/096702

[4] H. Paganetti, "Range uncertainties in proton therapy and the role of Monte Carlo simulations," *Phys. Med. Biol.*, vol. 57, no. 11, p. R99, 2012. Available: http://dx.doi.org/10.1088/0031-9155/57/11/R99

[5] A.-C. Knopf and A. Lomax, "In vivo proton range verification: a review," *Phys. Med. Biol.*, vol. 58, no. 15, p. R131, 2013. Available: http://dx.doi.org/10.1088/0031-9155/58/15/R131

[6] J. M. Verburg, K. Riley, T. Bortfeld, and J. Seco, "Energy- and time-resolved detection of prompt gamma-rays for proton range verification," *Phys. Med. Biol.*, vol. 58, no. 20, p. L37, 2013. Available: http://dx.doi.org/10.1088/0031-9155/58/20/L37

[7] J. M. Verburg and J. Seco, "Proton range verification through prompt gamma-ray spectroscopy," *Phys. Med. Biol.*, vol. 59, no. 23, p. 7089, 2014. Available: http://dx.doi.org/10.1088/0031-9155/59/23/7089

[8] I. Perali, A. Celani, L. Bombelli, C. Fiorini, F. Camera, E. Clementel, S. Henrotin, G. Janssens, D. Prieels, F. Roellinghoff, J. Smeets, F. Stichelbaut, and F. Vander Stappen, "Prompt gamma imaging of proton pencil beams at clinical dose rate," *Phys. Med. Biol.*, vol. 59, no. 19, p. 5849, 2014. Available: http://dx.doi.org/10.1088/0031-9155/59/19/5849

[9] M. Priegnitz, S. Helmbrecht, G. Janssens, I. Perali, J. Smeets, F. Vander Stappen, E. Sterpin, and F. Fiedler, "Measurement of prompt gamma profiles in inhomogeneous targets with a knife-edge slit camera during proton irradiation," *Phys. Med. Biol.*, vol. 60, no. 12, p. 4849, 2015. Available: http://dx.doi.org/10.1088/0031-9155/60/12/4849

[10] C. Richter, G. Pausch, S. Barczyk, M. Priegnitz, I. Keitz, J. Thiele, J. Smeets, F. V. Stappen, L. Bombelli, C. Fiorini, L. Hotoiu, I. Perali, D. Prieels, W. Enghardt, and M. Baumann, "First clinical application of a prompt gamma based in vivo proton range verification system," *Radioth Oncol*, 2016. Available: http://dx.doi.org/10.1016/j.radonc.2016.01.004

[11] D. Everett, J. Fleming, R. Todd, and J. Nightingale, "Gamma-radiation imaging system based on the Compton effect," *P I Electr Eng*, vol. 124, no. 11, p. 995, 1977. Available: http://dx.doi.org/10.1049/piee.1977.0203

[12] B.-H. Kang and J.-W. Kim, "Monte Carlo design study of a gamma detector system to locate distal dose falloff in proton therapy," *IEEE Trans Nucl Sci*, vol. 56, no. 1, pp. 46–50, 2009. Available: http://dx.doi.org/10.1109/TNS.2008.2005189

[13] S. Kabuki, K. Ueno, S. Kurosawa, S. Iwaki, H. Kubo, K. Miuchi, Y. Fujii, D. Kim, J. Kim, R. Kohara, O. Miyazaki, T. Sakae, T. Shirahata, T. Takayanagi, T. Terunuma, Y. Tsukahara, E. Yamamoto, K. Yasuoka, and T. Tanimori, "Study on the use of electron-tracking Compton gamma-ray camera to monitor the therapeutic proton dose distribution in real time," in *IEEE Nucl Sci Symp Conf Rec*, vol. J05-13, 2009, pp. 2437–2440. Available: http://dx.doi.org/10.1109/NSSMIC.2009.5402130

[14] M. H. Richard, M. Chevallier, D. Dauvergne, N. Freud, P. Henriquet, F. L. Foulher, J. M. Létang, G. Montarou, C. Ray, F. Roellinghoff, E. Testa, M. Testa, and A. H. Walenta, "Design study of a Compton camera for prompt γ imaging during ion beam therapy," in *IEEE Nucl Sci Symp Conf Rec*, 2009, pp. 4172–4175. Available: http://dx.doi.org/10.1109/NSSMIC.2012.6551055

[15] M. Frandes, A. Zoglauer, V. Maxim, and R. Prost, "A tracking Compton-scattering imaging system for hadron therapy monitoring," *IEEE Trans Nucl Sci*, vol. 57, no. 1, pp. 144–150, 2010. Available: http://dx.doi.org/10.1109/TNS.2009.2031679

[16] A. H. Compton, "A quantum theory of the scattering of X-rays by light elements," *Phys. Rev.*, vol. 21, no. 5, pp. 483–502, 1923. Available: http://dx.doi.org/10.1103/PhysRev.21.483

[17] X. Lojacono, "Image reconstruction for Compton camera with application to hadrontherapy," Ph.D. dissertation, INSA de Lyon, 2013. Available: https://tel.archives-ouvertes.fr/tel-01081066

[18] F. Hueso-González, "Nuclear methods for real-time range verification in proton therapy based on prompt gamma-ray imaging," Ph.D. dissertation, Technische Universität Dresden, 2016. Available: http://nbn-resolving.de/urn:nbn:de:bsz:14-qucosa-204988

[19] E. Hilaire, D. Sarrut, F. Peyrin, and V. Maxim, "Proton therapy monitoring by Compton imaging: influence of the large energy

spectrum of the prompt-γ radiation," *Phys Med Biol*, vol. 61, no. 8, p. 3127, 2016. Available: http://dx.doi.org/10.1088/0031-9155/61/8/3127

[20] J. D. Valentine, C. Bonnerave, and R. C. Rohe, "Energy-subtraction Compton scatter camera design considerations: a Monte Carlo study of timing and energy resolution effects," in *IEEE Nucl Sci Symp Conf Rec*, vol. 2, 1996, pp. 1039–1043. Available: http://dx.doi.org/10.1109/NSSMIC.1996.591539

[21] J. Smeets, "Prompt gamma imaging with a slit camera for real time range control in particle therapy," Ph.D. dissertation, Université Claude Bernard Lyon 1, 2012. Available: http://theses.ulb.ac.be/ETD-db/collection/available/ULBetd-10182012-123741/unrestricted/Thesis.pdf

[22] P. G. Ortega, I. Torres-Espallardo, F. Cerutti, A. Ferrari, J. E. Gillam, C. Lacasta, G. Llosá, J. F. Oliver, P. R. Sala, P. Solevi, and M. Rafecas, "Noise evaluation of Compton camera imaging for proton therapy," *Phys. Med. Biol.*, vol. 60, no. 5, p. 1845, 2015. Available: http://dx.doi.org/10.1088/0031-9155/60/5/1845

[23] T. Kormoll, F. Fiedler, S. Schöne, J. Wüstemann, K. Zuber, and W. Enghardt, "A Compton imager for in-vivo dosimetry of proton beams - a design study," *Nucl Instrum Methods Phys Res A*, vol. 626-627, no. 0, pp. 114–119, 2011. Available: http://dx.doi.org/10.1016/j.nima.2010.10.031

[24] H. Seo, J. H. Park, A. Ushakov, C. H. Kim, J. K. Kim, J. H. Lee, C. S. Lee, and J. S. Lee, "Experimental performance of double-scattering Compton camera with anthropomorphic phantom," *J Instrum*, vol. 6, no. 01, p. C01024, 2011. Available: http://dx.doi.org/10.1088/1748-0221/6/01/C01024

[25] G. Llosá, J. Cabello, S. Callier, J. Gillam, C. Lacasta, M. Rafecas, L. Raux, C. Solaz, V. Stankova, C. de La Taille, M. Trovato, and J. Barrio, "First Compton telescope prototype based on continuous LaBr3-SiPM detectors," *Nucl Instrum Methods Phys Res A*, vol. 718, no. 0, pp. 130–133, 2013. Available: http://dx.doi.org/10.1016/j.nima.2012.08.074

[26] J. Krimmer, J.-L. Ley, C. Abellan, J.-P. Cachemiche, L. Caponetto, X. Chen, M. Dahoumane, D. Dauvergne, N. Freud, B. Joly, D. Lambert, L. Lestand, J. Létang, M. Magne, H. Mathez, V. Maxim, G. Montarou, C. Morel, M. Pinto, C. Ray, V. Reithinger, E. Testa, and Y. Zoccarato, "Development of a Compton camera for medical applications based on silicon strip and scintillation detectors," *Nucl Instrum Methods Phys Res A*, vol. 787, pp. 98–101, 2015. Available: http://dx.doi.org/10.1016/j.nima.2014.11.042

[27] P. Thirolf, C. Lang, S. Aldawood, H. v.d. Kolff, L. Maier, D. Schaart, and K. Parodi, "Development of a Compton camera for online range monitoring of laser-accelerated proton beams via prompt-gamma detection," *EPJ Web of Conferences*, vol. 66, no. 11036, 2014. Available: http://dx.doi.org/10.1051/epjconf/20146611036

[28] M. McCleskey, W. Kaye, D. Mackin, S. Beddar, Z. He, and J. Polf, "Evaluation of a multistage CdZnTe Compton camera for prompt γ imaging for proton therapy," *Nucl Instrum Methods Phys Res A*, vol. 785, no. 0, pp. 163–169, 2015. Available: http://dx.doi.org/10.1016/j.nima.2015.02.030

[29] C. Golnik, D. Bemmerer, W. Enghardt, F. Fiedler, F. Hueso-González, G. Pausch, K. E. Römer, H. Rohling, S. Schöne, L. Wagner, and T. Kormoll, "Tests of a Compton imaging prototype in a monoenergetic 4.44 MeV photon field – a benchmark setup for prompt gamma-ray imaging devices," *J Instrum*, vol. 11, no. 06, p. P06009, 2016. Available: http://dx.doi.org/10.1088/1748-0221/11/06/P06009

[30] S. Kurosawa, H. Kubo, K. Ueno, S. Kabuki, S. Iwaki, M. Takahashi, K. Taniue, N. Higashi, K. Miuchi, T. Tanimori, D. Kim, and J. Kim, "Prompt gamma detection for range verification in proton therapy," *Curr Appl Phys*, vol. 12, no. 2, pp. 364–368, 2012. Available: http://dx.doi.org/10.1016/j.cap.2011.07.027

[31] P. Solevi, E. Muñoz, C. Solaz, M. Trovato, P. Dendooven, J. E. Gillam, C. Lacasta, J. F. Oliver, M. Rafecas, I. Torres-Espallardo, and G. Llosá, "Performance of MACACO Compton telescope for ion-beam therapy monitoring: first test with proton beams," *Phys Med Biol*, vol. 61, no. 14, p. 5149, 2016. Available: http://dx.doi.org/10.1088/0031-9155/61/14/5149

[32] J. C. Polf, S. Avery, D. S. Mackin, and S. Beddar, "Imaging of prompt gamma rays emitted during delivery of clinical proton beams with a Compton camera: feasibility studies for range verification," *Phys. Med. Biol.*, vol. 60, no. 18, p. 7085, 2015. Available: http://dx.doi.org/10.1088/0031-9155/60/18/7085

[33] D. Robertson, J. C. Polf, S. W. Peterson, M. T. Gillin, and S. Beddar, "Material efficiency studies for a Compton camera designed to measure characteristic prompt gamma rays emitted during proton beam radiotherapy," *Phys. Med. Biol.*, vol. 56, no. 10, p. 3047, 2011. Available: http://dx.doi.org/10.1088/0031-9155/56/10/010

[34] H. Krieger, *Strahlenphysik, Dosimetrie und Strahlenschutz*. Vieweg+Teubner Verlag, 1998, vol. 1, pp. 112–162. Available: http://dx.doi.org/10.1007/978-3-663-11534-2_4

[35] F. Hueso-González, A. K. Biegun, P. Dendooven, W. Enghardt, F. Fiedler, C. Golnik, K. Heidel, T. Kormoll, J. Petzoldt, K. E. Römer, R. Schwengner, A. Wagner, and G. Pausch, "Comparison of LSO and BGO block detectors for prompt gamma imaging in ion beam therapy," *J Instrum*, vol. 10, no. 9, p. P09015, 2015. Available: http://dx.doi.org/10.1088/1748-0221/10/09/p09015

[36] F. Hueso-González, C. Golnik, M. Berthel, A. Dreyer, W. Enghardt, F. Fiedler, K. Heidel, T. Kormoll, H. Rohling, S. Schöne, R. Schwengner, A. Wagner, and G. Pausch, "Test of Compton camera components for prompt gamma imaging at the ELBE bremsstrahlung beam," *J Instrum*, vol. 9, no. 05, p. P05002, 2014. Available: http://dx.doi.org/10.1088/1748-0221/9/05/P05002

[37] B. Kozlovsky, R. J. Murphy, and R. Ramaty, "Nuclear deexcitation gamma-ray lines from accelerated particle interactions," *Astrophys J Suppl Ser*, vol. 141, no. 2, p. 523, 2002. Available: http://dx.doi.org/10.1086/340545

[38] M. Zioga, M. Mikeli, A. Eleftheriou, C. Pafilis, A. N. Rapsomanikis, and E. Stiliaris, "ComptonRec: Mastering conic sections for a direct 3D Compton image reconstruction," in *IEEE Nucl Sci Symp Conf Rec*, vol. M4CP-266, 2015. Available: http://www.nss-mic.org/2015/ConferenceRecord/Details.asp?PID=M4CP-266

[39] R. Brun and F. Rademakers, "ROOT - An object oriented data analysis framework," *Nucl Instrum Methods Phys Res A*, vol. 389, no. 1–2, pp. 81–86, 1997. Available: http://dx.doi.org/10.1016/S0168-9002(97)00048-X

[40] F. Hueso-González, W. Enghardt, F. Fiedler, C. Golnik, G. Janssens, J. Petzoldt, D. Prieels, M. Priegnitz, K. E. Römer, J. Smeets, F. Vander Stappen, A. Wagner, and G. Pausch, "First test of the prompt gamma ray timing method with heterogeneous targets at a clinical proton therapy facility," *Phys. Med. Biol.*, vol. 60, no. 16, p. 6247, 2015. Available: http://dx.doi.org/10.1088/0031-9155/60/16/6247

[41] J. Smeets, F. Roellinghoff, D. Prieels, F. Stichelbaut, A. Benilov, P. Busca, C. Fiorini, R. Peloso, M. Basilavecchia, T. Frizzi, J. C. Dehaes, and A. Dubus, "Prompt gamma imaging with a slit camera for real-time range control in proton therapy," *Phys. Med. Biol.*, vol. 57, no. 11, p. 3371, 2012. Available: http://dx.doi.org/10.1088/0031-9155/57/11/3371

[42] A. K. Biegun, E. Seravalli, P. C. Lopes, I. Rinaldi, M. Pinto, D. C. Oxley, P. Dendooven, F. Verhaegen, K. Parodi, P. Crespo, and D. R. Schaart, "Time-of-flight neutron rejection to improve prompt gamma imaging for proton range verification: a simulation study," *Phys. Med. Biol.*, vol. 57, no. 20, p. 6429, 2012. Available: http://dx.doi.org/10.1088/0031-9155/57/20/6429

[43] J. Petzoldt, K. E. Roemer, W. Enghardt, F. Fiedler, C. Golnik, F. Hueso-González, S. Helmbrecht, T. Kormoll, H. Rohling, J. Smeets, T. Werner, and G. Pausch, "Characterization of the microbunch time structure of proton pencil beams at a clinical treatment facility," *Phys Med Biol*, vol. 61, no. 6, p. 2432, 2016. Available: http://dx.doi.org/10.1088/0031-9155/61/6/2432

[44] C. Golnik, F. Hueso-González, A. Müller, P. Dendooven, W. Enghardt, F. Fiedler, T. Kormoll, K. E. Römer, J. Petzoldt, A. Wagner, and G. Pausch, "Range assessment in particle therapy based on prompt γ-ray timing measurements," *Phys. Med. Biol.*, vol. 59, no. 18, p. 5399, 2014. Available: http://dx.doi.org/10.1088/0031-9155/59/18/5399

[45] M. Berger, J. Hubbell, S. S. abd J. Chang, J. Coursey, R. Sukumar, D. Zucker, and K. Olsen, "XCOM: Photon Cross Section Database, NIST Standard Reference Database 8 (XGAM)," *NIST*, 2010. Available: http://www.nist.gov/pml/data/xcom

[46] E. Muñoz, J. Barrio, A. Etxebeste, C. Lacasta, J. F. Oliver, C. Solaz, P. Solevi, M. Trovato, and G. Llosá, "Characterization and simulation results of a two/three-layer Compton telescope with LaBr3 and SiPMs," in *IEEE Nucl Sci Symp Conf Rec*, vol. M5BP-339, 2015. Available: http://www.nss-mic.org/2015/ConferenceRecord/GetCRFile.asp?PID=M5BP-339

[47] J. Stein, A. Kreuels, Y. Kong, R. Lentering, K. Ruhnau, F. Scherwinski, and A. Wolf, "Experiment and modeling of scintillation photon-counting and current measurement for PMT gain stabilization," *Nucl Instrum Methods Phys Res A*, vol. 782, no. 0, pp. 20–27, 2015. Available: http://dx.doi.org/10.1016/j.nima.2015.01.101

[48] C. E. Ordonez, W. Chang, and A. Bolozdynya, "Angular uncertainties due to geometry and spatial resolution in compton cameras," *IEEE Trans Nucl Sci*, vol. 46, no. 4, pp. 1142–1147, 1999. Available: http://dx.doi.org/10.1109/23.790848